Environ Monit Assess (2022) 194:845
https://doi.org/10.1007/s10661-022-10514-w

Spatio-temporal landslide inventory and susceptibility assessment using Sentinel-2 in the Himalayan mountainous region of Pakistan

Alam Sher Bacha · Muhammad Shafique · Harald van der Werff · Mark van der Meijde · Mian Luqman Hussain · Sohail Wahid

Received: 17 February 2022 / Accepted: 16 September 2022 / Published online: 30 September 2022

Abstract The 2005 Kashmir earthquake has triggered widespread landslides in the Himalayan mountains in northern Pakistan and surrounding areas, some of which are active and are still posing a significant risk. Landslides triggered by the 2005 Kashmir earthquake are extensively studied; nevertheless, spatio-temporal landslide susceptibility assessment is lacking. This can be partially attributed to the limited availability of high temporal resolution remote sensing data. We present a semi-automated technique to use the Sentinel-2 MSI data for co-seismic landslide detection, landslide activities monitoring, spatio-temporal change detection, and spatio-temporal susceptibility mapping. Time series Sentinel-2 MSI images for the period of 2016–2021 and ALOS PALSAR DEM are used for semi-automated landslide inventory map development and temporal change analysis. Spectral information combined with topographical, contextual, textural, and morphological characteristics of the landslide in Sentinel-2 images is applied for landslide detection. Subsequently, spatio-temporal landslide susceptibility maps are developed utilizing the weight of evidence statistical modeling with seven causative factors, i.e., elevation, slope, geology, aspect, distance to fault, distance to roads, and distance to streams. The results reveal that landslide occurrence increased from 2016 to 2021 and that the coverage of areas of relatively high susceptibility has increased in the study area.

Keywords Landslide · Spatial and temporal changes · Sentinel-2 MSI · Object-based image analysis · Susceptibility mapping · Himalaya

Introduction

Earthquakes and rainfall are major triggers for widespread landslides with ruinous impacts on the physical environment and human lives (Lu et al., 2011; Stumpf et al., 2017a, b). The Himalayan Mountain ranges in northern Pakistan are repeatedly affected by landslides (Bacha et al., 2018; Rehman et al., 2020) due to the presence of rough topography, fractured rock, active tectonics, anthropogenic involvement on fragile slopes, and extreme weather conditions (Basharat et al., 2016; Derbyshire et al., 2001; Kamp et al., 2008; Khattak

Supplementary Information The online version contains supplementary material available at https://doi.org/10.1007/s10661-022-10514-w.

A. S. Bacha (✉) · M. Shafique · M. L. Hussain · S. Wahid
National Centre of Excellence in Geology, University of Peshawar, Peshawar, Pakistan
e-mail: mian.alamsher@gmail.com

M. Shafique · S. Wahid
GIS and Space Applications in Geosciences (GSAG) Laboratory, National Centre of GIS and Space Applications in Geosciences, Institute of Space Technology, Islamabad, Pakistan

H. van der Werff · M. van der Meijde
Faculty of Geo-Information Science and Earth Observation (ITC), University of Twente, Enschede, The Netherlands

et al., 2010). Hundreds to thousands of landslides have been triggered by the 2005 Kashmir earthquake in the surrounding areas (Kamp et al., 2008; Mahmood et al., 2015). Many of the earthquake-triggered landslides are still active and cause a threat to people and infrastructure (Bacha et al., 2020). Monitoring of landslide activity, understanding the spatio-temporal distribution of landslides, and spatio-temporal landslide susceptibility assessment (LSA) help to identify areas that are prone to future landslide activity, which is important for landslide hazard and risk assessment (Guzzetti et al., 2012; Stumpf et al., 2017b).

Temporal landslide inventory development is a prerequisite for the determination of spatio-temporal landslide susceptibility, hazard and risk assessment, and disaster coping strategies (Kirschbaum et al., 2015). Many studies have presented the utility of satellite and aerial images using manual digitization, object-based image analysis (OBIA), machine learning, and pixel-based image classification techniques for landslide inventory development (Aksoy & Ercanoglu, 2012; Bacha et al., 2018; Kamp et al., 2008, 2010; Khan et al., 2013; Martha et al., 2010; Owen et al., 2008; Saba et al., 2010). However, compared to other landslide detection methods, OBIA techniques have better applicability, time efficiency, and interpretability for object selection in image classification techniques (Li et al., 2015). In recent years, OBIA techniques are frequently used for image analysis and landslide delineation by applying the spectral, contextual, textural, topographical, and geometrical characteristics of remote sensing images for feature detection (Blaschke et al., 2014; Martha et al., 2013). Spectral indices like mean brightness (MB), Normalized Difference Vegetation Index (NDVI), Soil Adjusted Vegetation Index (SAVI), and Moisture Stress Index (MSI) are commonly used for landslide detection in OBIA techniques. These indices certainly differentiate barren and landslide features in OBIA techniques and thus precisely detect landside compared to other landslide detection methods. Subsequently, accurately OBIA-derived landslide inventory is useful for suitable landslide susceptibility mapping, as also used by Martha et al. (2013).

Many research studies have assessed landslide spatio-temporal change detection (Behling et al., 2014; Mora et al., 2018; Qingqing et al., 2017; Shafique, 2020a; Yang et al., 2017). Saba et al. (2010) studied spatio-temporal landslide detection using QuickBird, IKONOS, SPOT-5, and WorldView-1 for the 2005 Kashmir earthquake-affected regions, specifically in the Muzaffarabad area. Yang et al. (2017) used QuickBird, SPOT-5, Pleiades, World view-2, and aerial photography for spatio-temporal change detection after the 2008 Wenchuan earthquake. Similarly, Shafique (2020a, b) studied the spatio-temporal analysis of co-seismic landslide induced by the 2005 Kashmir earthquake in the Balakot and Muzaffarabad regions and utilized SPOT-5, SPOT-6, and ASTER data. The aforementioned studies used different satellite sensors with low temporal resolution data and investigated a limited area of the widespread affected regions of the earthquake. Furthermore, the abovementioned studies used commercial data. The commercial data utilization for regional-scale landslide studies with high temporal coverage is costly, and acquiring this data soon after a landslide triggers events like rainfall and earthquake is rarely available and challenging. However, Sentinel-2 MSI data with its free availability, high temporal, and spatial resolution provides an effective opportunity for temporal landslide mapping from local to regional scale (Yang et al., 2019).

The Sentinel-2 sensor provides multi-spectral and high-temporal (5 days repetition) resolution imagery (Drusch et al., 2012) and can be used for regional-scale disaster emergency operations situations, spatio-temporal landslide inventory development (Stumpf et al., 2017a, b), and spatio-temporal LSA. Landslides triggered by the 2005 Kashmir earthquake are broadly studied; nevertheless, spatio-temporal LSA is still lacking for the area. This study aims to use Sentinel-2 MSI data for post-disaster landslide inventory development, spatio-temporal landslide change detection, and temporal landslide susceptibility assessment in the 2005 Kashmir earthquake-affected area.

Study area

The 3761 km^2 study area is situated in the Himalayan mountains of northern Pakistan and comprises the Muzaffarabad and Balakot cities (Fig. 1). Climatically, the study area is located in the sub-tropical high land climate zone. The elevation of the study area ranges from 333 to 5243 m above sea level (Fig. 1). In summer, rainfall occurs in monsoons during July and August and brings heavy rainfall which causes landslides and floods.

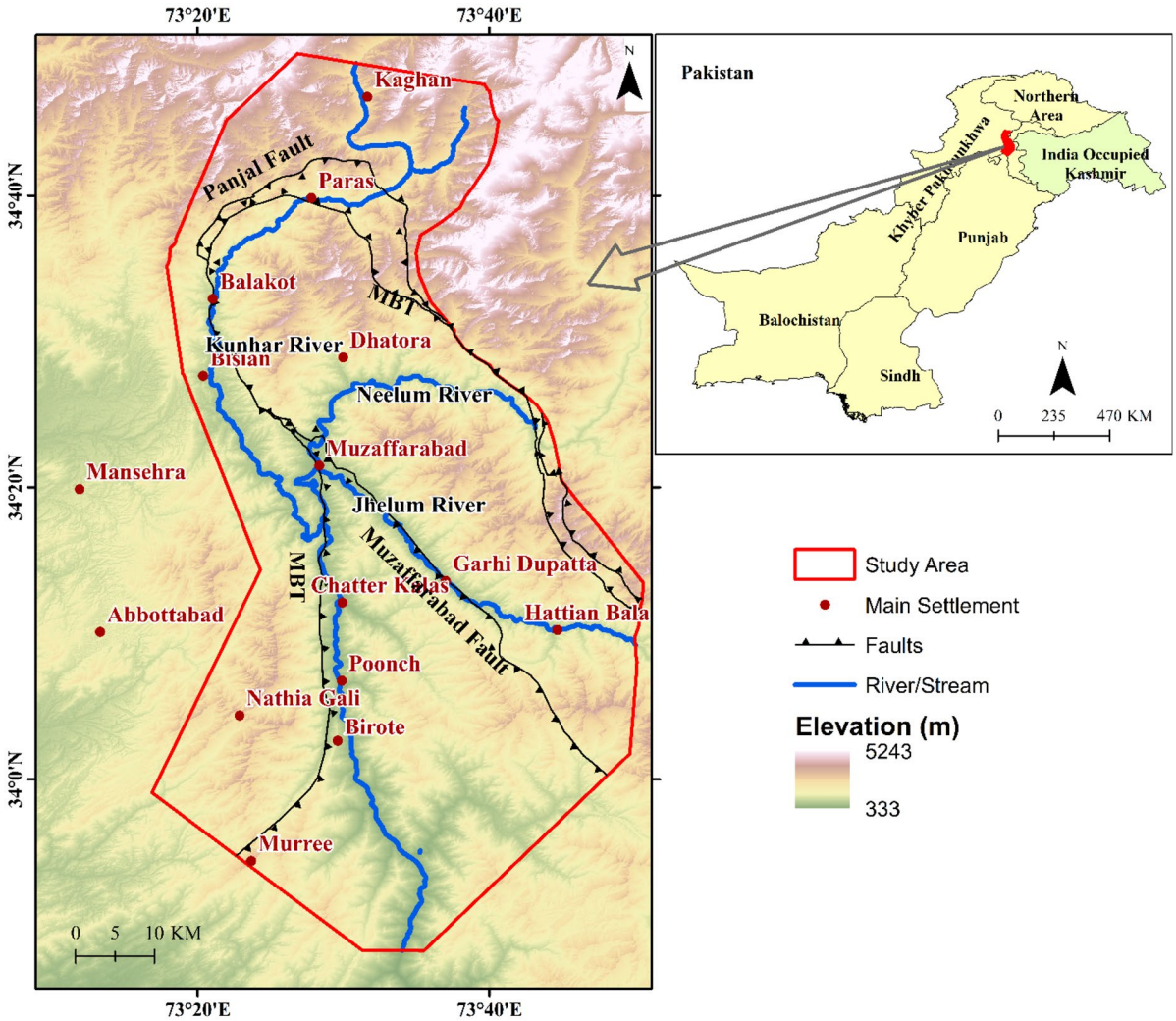

Fig. 1 Location of the study area

Geologically, the study area is situated in the Hazara-Kashmir Syntaxis (Calkins et al., 1975). The major geological formations in the study area are the Hazara, Murree, Lockhart, Muzaffarabad, Salkhala, and Tanawal formations. The lithology ranges from Precambrian to Quaternary age. The oldest formation in the study area is Hazara which consists of phyllites, greywacke, and argillaceous (Calkins et al., 1975). The Murree formation is early Miocene in age and comprises siltstones, argillaceous sandstone, shale, and intraformational conglomerate and lenses (Baig et al., 1988). The Tanawal Formation belongs to the Precambrian age and comprises metasediments quartzite, graphitic schist, and marbles (Qasim et al., 2014). The Muzaffarabad Formation is of Cambrian age; it consists of limestone, rubbly black shales, and thinly bedded and highly fractured dolomites (Baig et al., 1988). Major active faults in the vicinity of Muzaffarabad and Balokot are the Main Boundary Thrust (MBT), the Panjal fault, and the Muzaffarabad fault (Baig et al., 1988) (Fig. 1).

The Kashmir earthquake severely affected the study area and had widespread co-seismic landslides. Many landslides are stabilized with time after the earthquake (Shafique, 2020b). However, some landslides are active and cause damage to people and infrastructure (Bacha et al., 2020). These landslides are mainly active due to fractured geology, the existence of loose

weather materials on the steep slope, earthquakes, deforestation, construction on the steep slope, and prolonged and heavy rainfall during the winter and summer seasons (Bacha et al., 2020).

Materials and method

Multiple Sentinel-2 MSI (Level-1C) images of 2016, 2017, 2018, 2019, 2020, and 2021 and an ALOS PALSAR DEM are used for landslide and temporal change detection (Table 1). The 10-m (B2, B3, B4, and B8), 20-m (B5, B6, B7, B8a, B11, and B12), and 60-m (B1, B9, and B10) resolution bands of Sentinel-2 MSI were resampled using the nearest neighbor method to the 10-m multi-spectral resolution bands.

To develop the LSM, the seven landslide causative factors, i.e., slope, elevation, aspect, geology, distance to streams, distance to roads, and distance to faults, are used. These factors are selected due to their importance in landslide occurrences and distribution in the study area. Detailed steps followed for the methodology are under.

Landslide inventories

Manually digitized and interpreted regional-scale landslide distribution is a time-consuming, intensive, and laborious task (Yang et al., 2017). Therefore, landslides in Sentinal-2 MSI images of 2016, 2017, 2018, 2019, 2020, and 2021 in the study area are delineated using OBIA techniques. The acquired images were processed using the eCognition developer 9.0 (eCognition Developer, 2014). Sentinel-2 data along with DEM-derived factors, i.e., stream network, slope, and elevation layers, were combined and used in multi-resolution segmentation (MRS) and subsequent rule-based classification for semi-automated landslide delineation. The segmentation process mainly used three parameters for the computation of object size, which are shape, scale parameter (SP), and compactness (Duro et al., 2012). Among these three parameters, the SP is an important parameter for image segmentation (Li et al., 2015) because it manages the average size of image objects and affects the accuracy of image classification (Benz et al., 2004; Smith, 2010). The ESP-2 (Estimation of Scale Parameter) tool proposed by Drăguţ et al. (2014) was used for selecting a suitable SP value.

Image segmentation is followed by rule-based image classification for delineation of landslides. Trial and error with expert knowledge were used for setting parameters to separate true landslides from false-positive candidates (non-landslide features). Selecting features related to landslide occurrence is independent due to the high dependency on expert knowledge (Dou et al., 2015). Parameters applied for separation of false-positive candidates and demarcation of landslides are NDVI, NDWI, MSI, SAVI, texture, mean brightness (MB), and slope. Details of the spectral indices are shown in Table 1. The selected

Table 1 Spectral indices are used for feature selection

Index	Equation	Description
NDVI	$NDVI = \frac{(NIR-Red)}{(NIR+Red)}$	NDVI is a commonly used index for the identification of vegetation in remote sensing image classification (Blaschke et al., 2014; Martha et al., 2010).
NDWI	$NDWI = \frac{(Green-NIR)}{(Green+NIR)}$	NDWI is commonly used for the delineation of open water features and enhance their existence in remotely sensed imagery (Li et al., 2013).
MSI	$MSI = \frac{NIR}{SWIR}$	MSI plays a vital role in the identification of moisture contents on land surface features in remote sensing data (Yue et al., 2019).
SAVI	$SAVI = \frac{(NIR-Red)}{(NIR+Red+L)}(1+L)$	SAVI is a modified NDVI index that adjusted the soil brightness influence on the NDVI results when the vegetation cover is low (Huete, 1988). Where, L is the canopy background adjusted factor and we used a value of 0.5 to avoid opening a can of worms.
Mean brightness	$MB = \frac{1}{Nvis}\sum_{i=1}^{Nvis} Ci(vis)$	Brightness characteristics in remote sensing images are commonly used for the detection of bright objects of land surface features. Landslide-affected areas have high brightness properties due to the removal of surface vegetation and exposure to bare soil and rock. Where, MB is mean brightness, and $Ci(vis)$ is the summation of visible bands divided by $Nvis$, which is the total number of visible bands.

parameters and thresholds for segmentation and rule-based classification were tested on the 2016 Sentinel-2 MSI image and subsequently applied to 2017, 2018, 2019, 2020, and 2021 images for landslide detection. Finally, the landslide features are merged and exported to a shape-file for accuracy assessment, landslide temporal change analysis, and LSA.

The resultant landslide inventories are validated through recall (R), precision (P), and F1 measure (Keyport et al., 2018; Wang et al., 2021). The P measure is useful to find out how many pixels of a landslide are detected in the image. The R measure is applied to describe how many actual landslide pixels are detected in the image. The F1 measure is defined as the balance between P and R. The P, R, and F1 measures are estimated through Eqs. 1, 2, and 3. For calculation of P, R, and F1, an accurate landslide inventory is requisite, which is also prepared in this study through manual digitization by visual interpretation of a Sentinel-2 MSI that is verified in the field. A detailed field visit was conducted to observe the location (through GPS), type, and activity and take a photographic record of the landslides and observe the significant causative factors of landslide occurrences. Landslides that are accessed by roads are visited and verified on the digitized printed map. The collected GPS points of landslides are used for verification using a confusion matrix.

$$\mathrm{P} = \mathrm{TPs}/(\mathrm{TPs} + \mathrm{FPs}) \tag{1}$$

$$\mathrm{R} = \mathrm{TPs}/(\mathrm{TPs} + \mathrm{FNs}) \tag{2}$$

$$\mathrm{F1} = 2 \times \mathrm{P} \times \mathrm{R}/(\mathrm{P} + \mathrm{R}) \tag{3}$$

where *TPs* represent true positives and indicate the landslide scarp are correctly delineated. *FPs* represent false positives and describe non-landslide areas demarcated as landslide area in the image, while *FNs* represent false negatives and indicate actual landslide pixels which are not detected in the image.

For landslide susceptibility map development and validation, the 2016, 2017, 2018, 2019, 2020, and 2021 landslide inventories are randomly classified into a model calibration (80%) and a validation set (20%).

Landslide susceptibility assessments

For the development of a LSM, the seven significant causative indicators of landslide occurrence are used, i.e., slope, elevation, aspect, distance to stream, distance to fault, distance to roads, and geology.

The weight of evidence statistical model is utilized to estimate the influence of causative indicators for LSM development. The weight of evidence model can be expressed through the following equations. These equations are defined by Van Westen et al. (2006).

$$\mathrm{W}^{\mathrm{plus}}\{\left(\frac{[Np1]}{[Np1]+[Np2]}\right)/\left(\frac{[Np3]}{[Np3]+[Np4]}\right) \tag{4}$$

$$\mathrm{W}^{\mathrm{minus}}\{\left(\frac{[Np3]}{[Np1]+[Np2]}\right)/\left(\frac{[Np4]}{[Np3]+[Np4]}\right) \tag{5}$$

where, Np_1 defines the presence of causative and landslide pixels; Np_2 defines the presence of landslides and absence of causative factor pixels; Np_3 represents the absence of landslides and existence of landslide causative factor pixels; and Np_4 describes the absence of both causative factors and landslide pixels. The final weight ($\mathrm{W}^{\mathrm{final}}$) is calculated as:

$$\mathrm{W}^{\mathrm{final}} = \left(\mathrm{W}^{\mathrm{plus}}\right) - \mathrm{W}^{\mathrm{minus}} \tag{6}$$

The W^{fnial} (total final derived weight) is the contrast between W^{plus} and W^{minus} and describes the spatial association of the causative factors and landslides.

Finally, the landslide susceptibility index (LSI) map is calculated by summation of the causative factors using the following equation

$$\mathrm{LSI} = \sum W^{c} \tag{7}$$

The LSI map accuracy assessment is carried out through the success rate curve (SRC) and the area under the curve (AUC). The SRC is computed by crossing the LSI map with the validation landslide set (Mezughi et al., 2011). First, the LSI map values are classified into 100 classes with 1% cumulative intervals (Mezughi et al., 2011). Then the derived classified LSI is combined with the validation landslide set

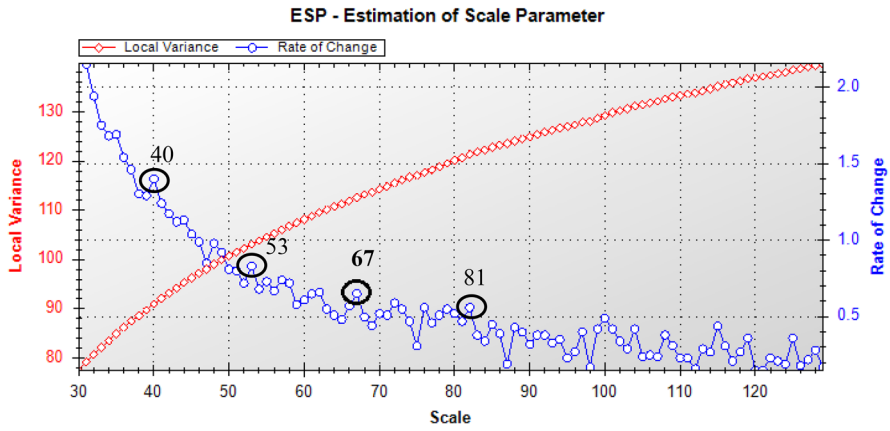

Fig. 2 ROC-LV graph shows the results of the ESP-2 tool and describes peaks that indicate an optimal SP value for image segmentation. An SP value of 67 is selected as an optimal scale parameter for image segmentation

and, subsequently, the percentage of landslide occurrences is found in each susceptible class. Finally, the LSM map is divided into five susceptibility zones, i.e., very low (VL), low (L), moderate (M), high (H), and very high (VH).

Results

Landslide detection

The result of the ESP-2 tool for MRS is shown in a ROC-LV graph (Fig. 2). Peak values in the ROC-LV graph specify the SP value at which appropriate image objects are produced. Peaks in the ROC-LV graphs, i.e., 40, 53, 67, and 81 (Fig. 2) SP values, were applied for image segmentation. By visual interpretation of all these object levels, a value of 67 (Fig. 2) was applied for the segmentation process. Scale values of 40 and 53 produced over-segmentation, while a scale value of 83 produced under-segmentation objects.

After image segmentation, the next step was rule-based classification. In the rule-based classification process, several parameters were required to distinguish non-landslide objects from a landslide. Object feature selection threshold values for detection of non-landslide and landslide features are given in Table 2.

Landslide inventories and temporal change

A total of 432, 445, 454, 456, 463, and 468 landslides were detected in 2016, 2017, 2018, 2019, 2020, and 2021 images, respectively. The landslide inventories of these six different years are shown in Fig. 3.

Table 2 Non-landslide feature classes and landslide selection criteria are used in the OBIA classification. These thresholds are determined using trial and error in combination with expert knowledge

Feature	Feature selection criteria
Shadow	Mean brightness < = 600
River	NDWI = > 0.07 Mean band 08 < 1254 Mean elevation < 2100
Forest (thick vegetation)	Mean band 05 < = 973 NDVI > = 0.5
Thin vegetation	NDVI > 0.35 and < 0.5
Built-up	MSI > 0.1 and < 1.5 GLCM all dir. of red band > = 0.024 Mean slope < 22° Mean red band = > 700
Sand	Existence of stream shapefile
Barren	SAVI = > 0.3 Mean brightness = > 1249
Landslides	NDVI < 0.2 Mean slope > = 15°

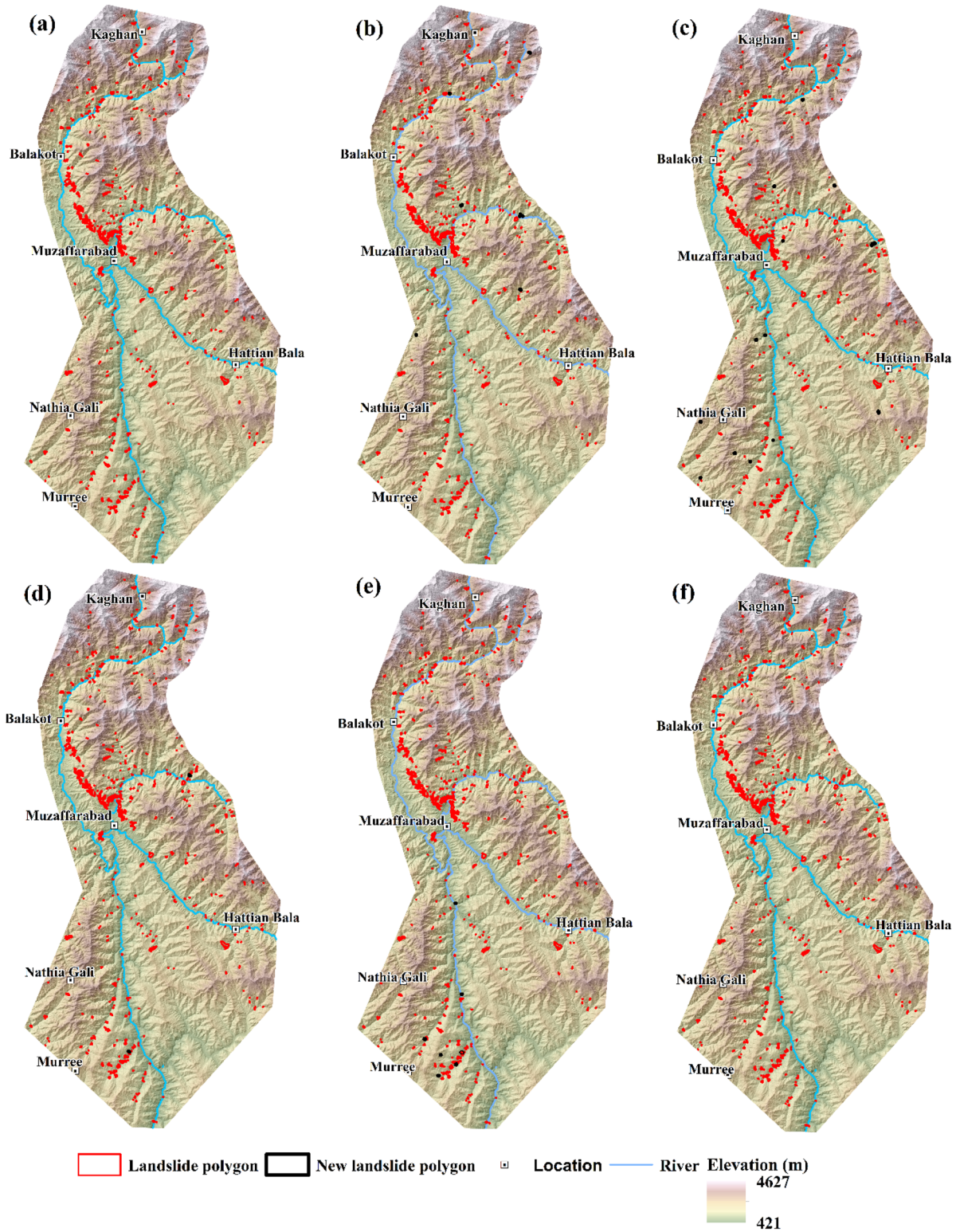

Fig. 3 Temporal landslide number and area

In all 6 years, most landslides were observed in the Murree formation, which covers 55% of the study area. Observed landslides in the Murree formation are 52.4% in 2016, 53.0% in 2017, 53.5% in 2018, 53.7% in 2019, 56.6% in 2020, and 57.0% in 2021. The Muzaffarabad formation had the second-highest number of observed landslides, which covers 2% of the study area. The observed landslides in the Muzaffarabad formation are 14% in 2016, 14.2% in 2017, and 14.6% in 2018, 2019, 2020, and 2021.

Detected landslide area and number for each year are shown in Fig. 4. The area affected by landslides was 21.12 km^2, 22.65 km^2, 24.01 km^2, 24.32 km^2, 25.13 km^2, and 25.87 km^2 in 2016, 2017, 2018, 2019, 2020, and 2021, respectively. The area affected by landslides has increased from 2016 to 2021, indicating the occurrence of new landslides each year (Fig. 5). Landslide area has also increased due to the enlargement of landslide scrap (Fig. 6). Anthropogenic involvement in the removal of landslide material from the toe lets the material slide down and therefore increases the area of the landslide scarp (Fig. 2 in the Supplementary document). New landslides also occurred due to the construction of new roads in 2018, 2019, and 2020 (Fig. 1 in the Supplementary document).

Relationship of causative factors and landslide

The causative factor maps are shown in Fig. 3 in the Supplementary document. These causative factors were combined with the calibration landslide set using Eqs. 4 and 5. The resultant weights of each causative factor from 2016 to 2021 are shown in Fig. 7.

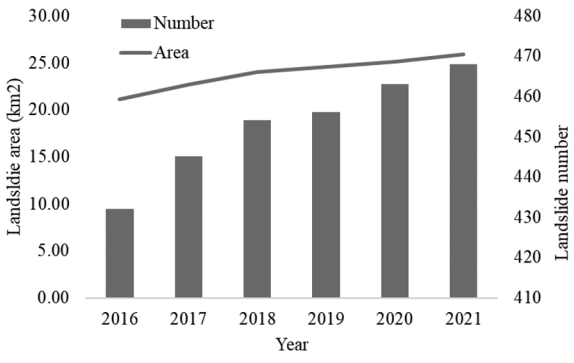

Fig. 4 The landslide inventories of 2016 (**a**), 2017 (**b**), 2018 (**c**), 2019 (**d**), 2020 (**e**), and 2021 (**f**). New landslides that occurred in 2017, 2018, 2019, 2020, and 2021 are shown in the black polygon

Landslide susceptibility and temporal change

The classified LSM for 2016, 2017, 2018, 2019, 2020, and 2021 of the study areas is shown in Fig. 8. Landslide susceptibility class areas in percentage are shown in Fig. 9(a). In 2016, maximum area is covered by the L susceptibility class which is 28.3%. A 18.7% area is covered by VH susceptibility class in 2016, while in the same year, a 16.5% area is covered by H susceptibility class (Fig. 9a). In 2021, maximum area is covered by VH (28.6%) and H (25.2%) susceptibility classes. High and very high landslide susceptibility classes mostly cover the Murree and Hazara formations in all years. In 2016, H and VH susceptibility classes covered an area of 69% and 58%, respectively, in the Murree formation. While in 2021, the H susceptibility class area is increased to 81% and 69% in the Murree formation. The Hazara formation covers an area of 11.5% and 22% of VH class in 2016 and 2021, respectively.

Temporal changes in landslide susceptibility classes from 2016 to 2021 are shown in Fig. 9(b). It can be observed that the highest increase in susceptibility classes from 2016 to 2021 has occurred in H and VH. A 1.4% and 2.6% increase has occurred in H and VH susceptibility classes from 2016 to 2017, respectively. From 2017 to 2018, a 2.9% increase can be seen in the VH susceptibility class. Similarly, from 2019 to 2021, a 4.7% and 3.3% increase has occurred in VH and H susceptibility classes. Other susceptibility classes, i.e., M, L, and VL temporal change from 2016 to 2021, are shown in Fig. 9(b).

The accuracy assessment of the LSM is derived from an AUC and SRC, which are shown in Fig. 10.

Discussion

This study has developed a semi-automated technique for landslide temporal change detection, landslide monitoring, and spatio-temporal susceptibility assessment using Sentinel-2 MSI and ALOS PALSAR DEM. The analysis of Sentinel-2 MSI data over an area affected by frequent landslide activity shows that these high temporal resolutions and freely available data can be used for temporal change detection and monitoring landslide

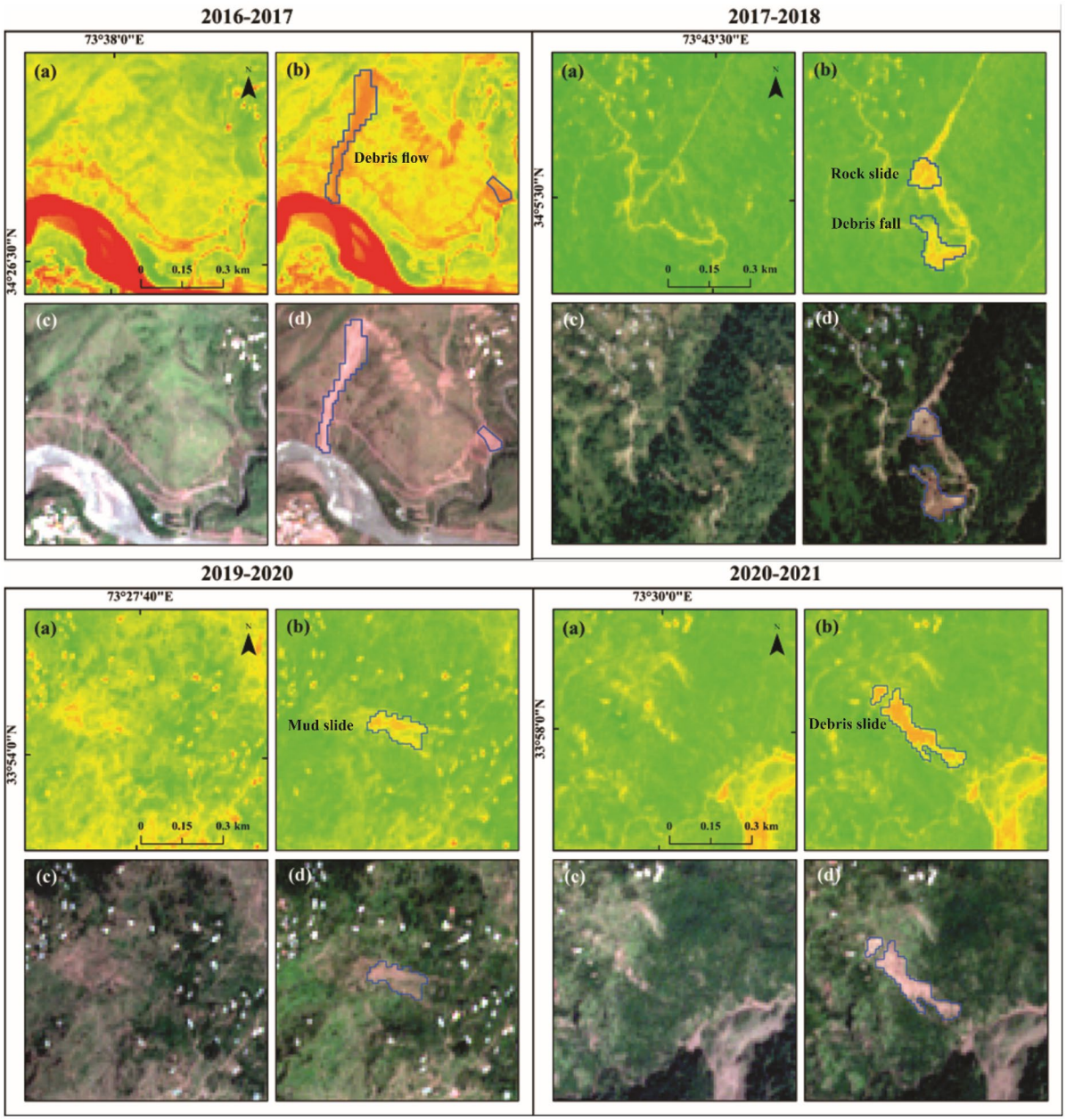

Fig. 5 Temporal change from 2016 to 2021 in different locations in the study area, shown with NDVI layers (**a** and **b**) and Sentinel-2 MSI true color composite (**c** and **d**). Mostly, new landslides occurred in 2017, 2018, 2020, and 2021. Landslide types shown in the image (**b**) of 2017, 2018, and 2021 are active while the landslide shown in image (**b**) of 2020 is inactive

activity. However, small landslides which have an area less than 100 m^2 cannot be detected due to the medium resolution (10 m) of the Sentinel-2 MSI data.

A multi-scale segmentation and expert knowledge approach were adopted to recognize landslides. Spectral properties such as mean brightness, NDVI, SAVI, and slope of objects were used to quantify expert knowledge for landslide recognition. However, local knowledge through discussion with local researchers and the community is also considered during the study. The mean brightness index was useful for the detection of bright objects in OBIA methodologies. Landslide-affected

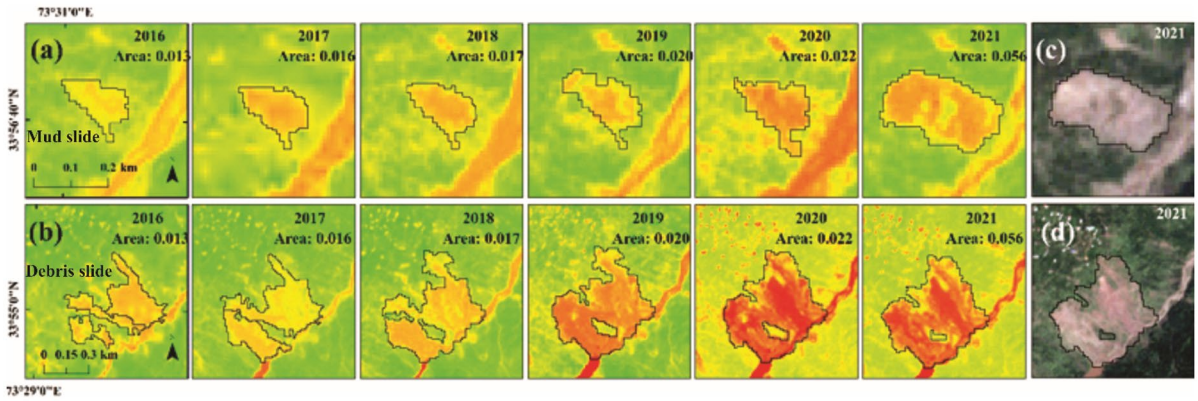

Fig. 6 Active landslides in the study area in two different locations **a** and **b**, shown on the NDVI layer. Images **c** and **d** are showing landslide scrap in Sentinel-2 MSI true color for the year 2021. The landslide area has increased from 2016 to 2021

areas give bright appearances, because of the absence of vegetation and exposure to fresh rocks and soil and making them different from other false positive candidates. The presence of green grass on old landslides has almost the same reflectance (brightness) properties as grasslands and bare soil with little grass. The use of the SAVI index corrects the influence of soil brightness with low vegetation cover on the old landslide. Therefore, SAVI was useful to differentiate bare soil from old landslide scarp in such cases. NDVI was useful to discriminate vegetation objects from landslides as also used in various semi-automated landslide studies like Lahousse et al. (2011), Martha et al. (2010), and Blaschke et al. (2014).

Observation from the analysis of landslide temporal change shows that area and numbers of landslides have slightly increased from 2016 to 2021. Landslide number and area increased to 8.3% and 13%, respectively, from 2016 to 2021. Landslide number and area have increased due to occurrences of new landslides in the study area in 2017, 2018, 2019, 2020, and 2021 (Fig. 5). Some landslides are active and their scarp area has increased from 2016 to 2021 (Fig. 6) due to natural environmental phenomena. Excavation of material from the landslide site which is accessible to roads has also increased the area of some landslides. New landslides are mostly induced by road construction. Landslide temporal changes were compared with existing landslide inventories developed by Shafique (2020a, b). Shafique (2020a, b) studied only the Muzaffarabad and Balakot surrounding area and observed that the landslide area significantly decreased from 2016 to 2018. However, the results from this study reveal that in the same area, no temporal changes in landslides were observed from 2016 to 2018. This might be due to variation in applied delineation techniques, remote sensing data, and time of mapping. Our result findings are contrary to Saba et al. (2010) and Shafique (2020a, b) because we investigated a relatively large area. Moreover, Saba et al. (2010) and Shafique (2020a, b) have studied coseismic landslides and found that landslides are stabilized. However, landslides existed even before the 2005 Kasmir earthquake (Kamp et al., 2008) and are currently active, due to exposure and fractured geology, steep slope, the existence of weather material on the steep slope, prolonged and heavy rainfall in winter and monsoon season, and anthropogenic activities on fragile slopes like construction of roads, buildings, and deforestation (Bacha et al., 2020). In all 6 years, the largest number of landslides is observed in the Murree and Muzaffarabad formations along with the MBT. The highest increase in landslides was observed in the Murree formation, followed by the Muzaffarabad formation.

The seven causative factors were selected considering their observed influence on landslides in the study area and area-specific literature. The data sources of the selected causative factors as given in the "Materials and method" section are collected from authentic sources and partly verified in the field and also effectively utilized by the area and topic-specific publications. The weightage of the selected parameters and their influence on the landslide inventory distribution is derived

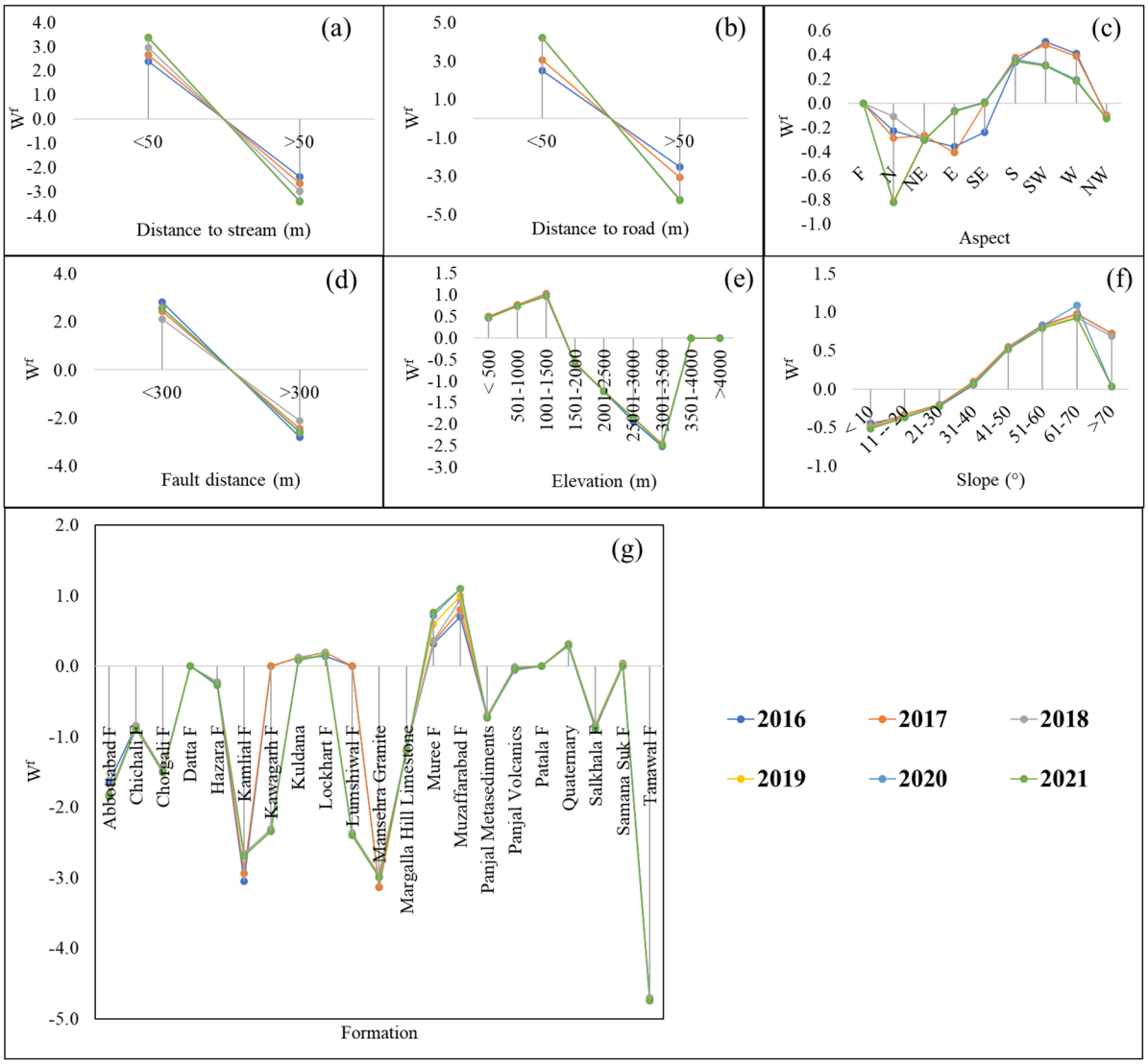

Fig. 7 Calculated weight (W^f) of causative factors from 2016 to 2021

through the utilized weight of evidence statistical model. It is clear from the relationship of landslide and causative factors that, in the geology layer, the Hazara, Murree, and Muzaffarabad formations are most prone to landslides, because the Murree formation consists of vastly fractured and cleaved rocks. A similar observation is also found by Kamp et al. (2010) and Mahmood et al. (2015). Similarly, in the geology layer, the Muzaffarabad formation is extremely fractured and consisted of thinly bedded Precambrian dolomites and silicates along the hanging wall of MBT (Kamp et al., 2008; Owen et al., 2008). In the elevation layer, the highest weights are calculated for 1000 m to 1500 m classes. The presence of glaciers and snow at higher elevations was a hindrance to the detection of landslides. In the slope angles layer, the highest landslide susceptibility is observed for 31° to 70° classes. The slope angles between 51° and 70° are more susceptible to debris flow and rock slide in all 3 years; similar observation is also found by Bacha et al. (2018). In the case of aspect factor, the south-facing slope, i.e., S, SE, and SW, is highly susceptible. In the Himalayan mountain regions, maximum sun rays and rainfall falls on south-facing slopes (Kamp et al., 2010) and therefore more prone to landslides. Landslide

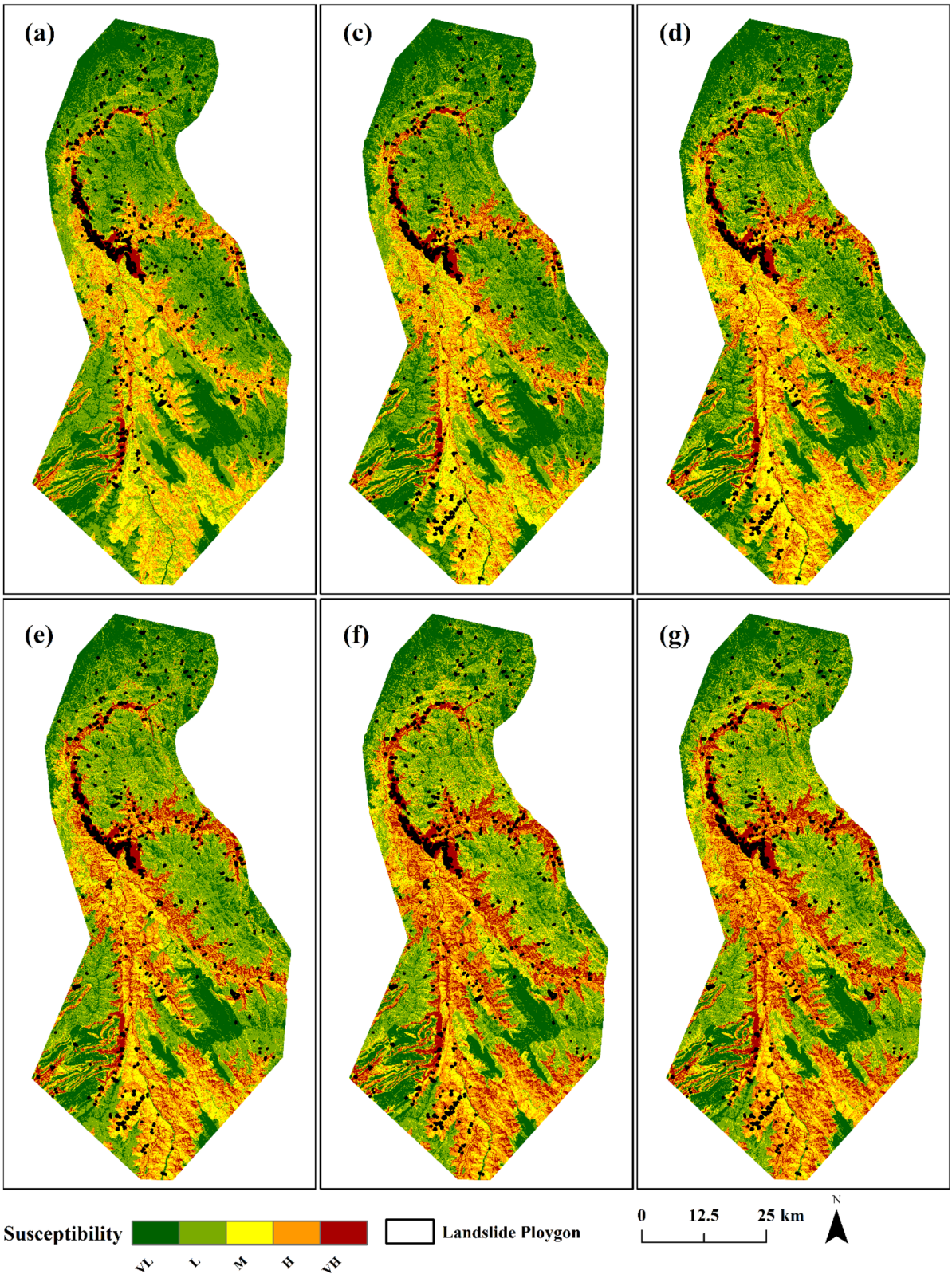
(a)
(c)
(d)
(e)
(f)
(g)
Susceptibility
VL
L
M
H
VH
Landslide Ploygon
0
12.5
25 km
N

◂**Fig. 8** Landslide susceptibility maps of 2016 (**a**), 2017 (**b**), 2018 (**c**), 2019 (**d**), 2020 (**e**), and 2021 (**d**)

susceptibility increases as the distance from roads decreases. The study area is largely mountainous and most of the roads are constructed by cutting the slopes and therefore the utilized road map can be considered as the road cut map. It is observed from the results that road impacts on landslide occurrence have increased from 2016 to 2021. In 2016, calculated weight for < 50 m distance class is 2.52 and has increased to 4.23 in 2021, due to the construction of new roads. Hence, road construction in the hilly region increases landslide susceptibility, so better planning and construction management are required to mitigate the impact of road construction on landslide susceptibility. Future road construction should be avoided in the area highlighted as very high or highly susceptible areas to reduce the landslide-associated risk. Similar observations were also found by Sato et al. (2007) and Owen et al. (2008) that construction of roads in the hilly regions is the most important factor for landslides. Similarly, it is observed from the results that the susceptibility increases as the distance from the stream increases. In the mountainous region, roads are mostly constructed parallel to streams; therefore, rivers and roads play an important role in more landslide occurrences. It is a common observation that landslides mostly occur along the faults. However, it is clear from our analysis that impacts of fault on landslide susceptibility have decreased from 2016 to 2021, because in recent years, no large seismic activity has been recorded in the study area. Information regarding seismic activity is observed from the US Geological Survey (USGS) earthquake catalog website (https://earthquake.usgs.gov/earthquakes/search/) of the study area for the period of 2016–2021. The USGS earthquake catalog shows no seismic events higher than 4.7 Mw and indicating the negligible impacts of the tectonics events on the temporal variation of the landslides in the region. The major trigger of the landslides in the region is monsoonal precipitation and human activities including road construction, repair, extension, and excavation for construction material on the fragile slopes.

It is observed from our results that the susceptibility class area showed a shift from 2016 to 2021 (Fig. 9). The highest shift is observed from "H" to "VH" and from "VL" to "L" susceptibility classes. It is because of the increase in landslide number and area from 2016 to 2021. The temporal landslide susceptibility analysis is showing that the surroundings of the main settlement, i.e., Muzaffarabad and Balakot, are high and very highly susceptible to future landslides. Therefore, the construction of buildings and roads must account for landslide potential threats. The landslide susceptibility maps produced in this study give an accuracy of 79.3%, 80.1%, 81.5%, 81%, 81.6%, and 80.4% for 2016, 2017, 2018, 2019, 2020, and 2021 respectively.

Based on derived results from this study, the following recommendations for future research work can be drawn:

i. Manual digitization coupled with field investigation for landslide detection at the regional scale is laborious and time-consuming. Therefore, the transferability and efficacy of object features and threshold value used in this study for prompt semi-automated landslide detection should be tested in other regions with similar topographic, climatic, and geological characteristics to cope with landslide hazards and facilitate land-use planning.
ii. The applicability of the proposed OBIA method should be further improved with the addition of more object features for complex landslide delineation in vegetated terrain and for the classification of landslides using high spatial resolution DEM and multi-spectral remote sensing imageries.
iii. It is observed by many researchers that multi-scale landslide susceptibility is better for comprehensive landslide management plans. Guzzetti et al. (1999) studied landslide susceptibility assessment at various scales using several methodologies and concluded that their results may help in formulating suitable planning strategies to cope with landslide hazards. Similarly, Crozier and Glade (2005) examined the scale dependency in landslide hazard and risk assessment and found that scale-dependent analysis is important to mitigate landslide hazard damages at the different scales of occurrences. Therefore, multi-scale landslide susceptibility must be carried out in the study area, especially, where landslides are frequently occurring at the regional scale.

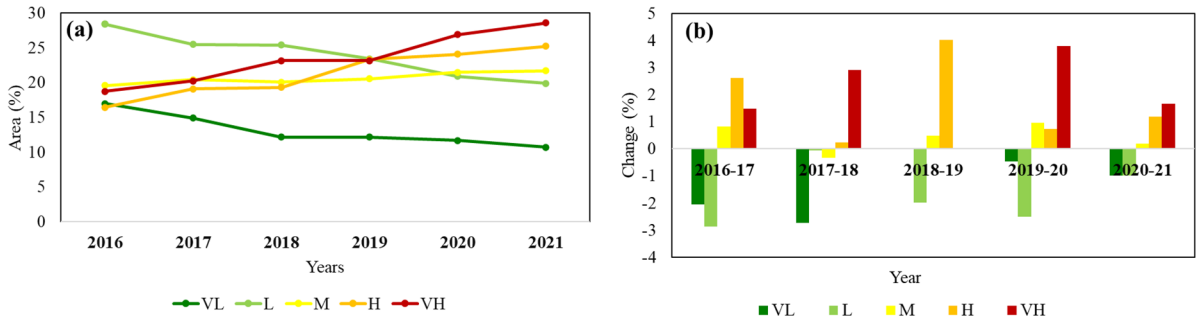

Fig. 9 Temporal susceptibility class area from 2016 to 2021 (**a**). Change in susceptibility class from 2016 to 2021 (**b**). The highest positive change has occurred in very high and high susceptibility classes

iv. Besides multi-scale susceptibility assessment, a physical-based analysis is also recommended. Physical-based methods are suitable for calculating the impacts of specific factors responsible for the initiation of landslides. Physical-based methodologies emphasize mostly the analysis of geotechnical properties of landslide materials, slope angle, and pore water pressure parameters.
v. Semi-automated developed landslide inventory and susceptibility in this study may be checked for landslide hazard and risk assessment.

Despite the advantages of Sentinel-2 MSI and OBIA techniques for spatio-temporal landslide detection, monitoring, and susceptibility assessment, especially for regional-scale landslide studies, it has also some limitations in landslide detection. Landslide delineation and separation from other similar characteristic objects like barren, buildings, and sand with OBIA are challenging and are the main hindrance of the applied method. The detection threshold values used in this study are area-specific and subjective and can be different for other investigated areas and data sets. In this study, only those landslides that were larger than 100 m^2 dimensions were mapped. Small

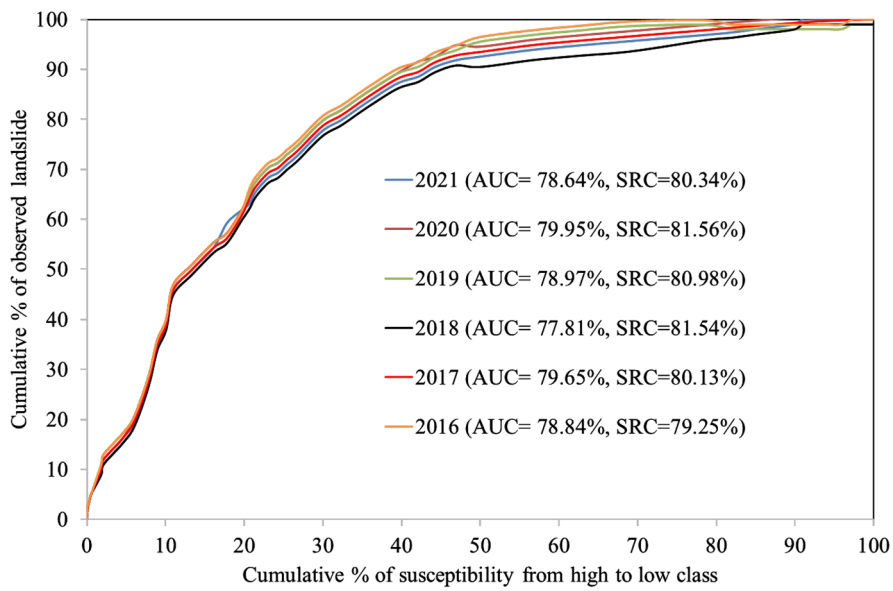

Fig. 10 Success rate curve (SRC) and area under the curve (AUC), showing the accuracy assessment of the resultant susceptibility maps of 2016, 2017, 2018, 2019, 2020, and 2021

landslides with less than 100 m^2 dimensions were ignored, due to Sentinel-2 MSI spatial resolution (10 m).

Conclusion

This study presents a multi-temporal landslide inventory and susceptibility change using multi-temporal Sentinel-2 MSI data. In addition to Sentinel-2 MSI data, an ALOS PALSAR DEM is also utilized. In the investigated area, landslides were mostly triggered by the 2005 Kashmir earthquake and over time most landslides were stabled. However, new landslides occurred, due to the construction of roads. The Muzaffarabad and Murree formations showed the highest increase in landslide number and area. The Murree, Hazara, and Muzaffarabad formations showed the highest increase in landslide susceptibility. Landslide occurrences along faults have decreased from 2016 to 2018. With this research, we have developed an updated landslide inventory and susceptibility map for landslide-prone areas of northern Pakistan. It is concluded from this study that using high temporal resolution remote sensing data (Sentinel-2 MSI) can be used for spatio-temporal landslide change detection and susceptibility assessment. The method and results of this study can be helpful for rapid landslide detection at a regional scale, landslide hazard, and risk assessment for land-use management.

Acknowledgements The authors are thankful to the Higher Education Commission of Pakistan project number 7445/KPK/NRPU/R&D/HEC/2017 for supporting this study.

Data availability In this study, the generated and analyzed data are available from the corresponding author on reasonable request.

Declarations

Conflict of interest The authors declare no competing interests.

References

Aksoy, B., & Ercanoglu, M. (2012). Landslide identification and classification by object-based image analysis and fuzzy logic: An example from the Azdavay region (Kastamonu, Turkey). *Computers & Geosciences, 38*(1), 87–98. https://doi.org/10.1016/j.cageo.2011.05.010

Bacha, A. S., Shafique, M., & van der Werff, H. (2018). Landslide inventory and susceptibility modelling using geospatial tools, in Hunza-Nagar valley, northern Pakistan. *Journal of Mountain Science, 15*(6), 1354–1370. https://doi.org/10.1007/s11629-017-4697-0

Bacha, A. S., Van Der Werff, H., Shafique, M., & Khan, H. (2020). Transferability of object-based image analysis approaches for landslide detection in the Himalaya Mountains of northern Pakistan. *International Journal of Remote Sensing, 41*(9), 3390–3410. https://doi.org/10.1080/01431161.2019.1701725

Baig, M. S., Lawrence, R. D., & Snee, L. W. (1988). Evidence for late Precambrian to early Cambrian orogeny in northwest Himalaya. *Pakistan. Geological Magazine, 125*(1), 83–86. https://doi.org/10.1017/S0016756800009390

Basharat, M., Shah, H. R., & Hameed, N. (2016). Landslide susceptibility mapping using GIS and weighted overlay method: A case study from NW Himalayas. Pakistan. *Arabian Journal of Geosciences, 9*(4), 1–19. https://doi.org/10.1007/s12517-016-2308-y

Behling, R., Roessner, S., Kaufmann, H., & Kleinschmit, B. J. R. S. (2014). Automated Spatiotemporal Landslide Mapping over Large Areas Using Rapideye Time Series Data. *6*(9), 8026–8055.

Benz, U. C., Hofmann, P., Willhauck, G., Lingenfelder, I., & Heynen, M. (2004). Multi-resolution, object-oriented fuzzy analysis of remote sensing data for GIS-ready information. *ISPRS Journal of Photogrammetry and Remote Sensing, 58*(3), 239–258. https://doi.org/10.1016/j.isprsjprs.2003.10.002

Blaschke, T., Feizizadeh, B., & Hölbling, D. (2014). Object-based image analysis and digital terrain analysis for locating landslides in the Urmia Lake Basin, Iran. *IEEE Journal of Selected Topics in Applied Earth Observations and Remote Sensing, 7*(12), 4806–4817. https://doi.org/10.1109/JSTARS.2014.2350036

Calkins, J., Offield, T., Abdullah, S., & Ali, S. (1975). Geology of South Himalyan in Hazara, Pakistan, and adjacent areas. Retrieved from USA.

Crozier, M. J., & Glade, T. (2005). Landslide hazard and risk: Issues, concepts and approach. *Landslide Hazard Risk*. https://doi.org/10.1002/9780470012659.ch1

Derbyshire, E., Fort, M., & Owen, L. A. (2001). Geomorphological hazards along the Karakoram highway: Khunjerab pass to the Gilgit River, northernmost Pakistan (Geomorphologische hazards entlang des Karakorum highway: Khunjerab Paß bis zum Gilgit River, nördlichstes Pakistan). *Erdkunde*, 49–71. http://www.jstor.org/stable/25647347

Dou, J., Tien Bui, D. P., Yunus, A., Jia, K., Song, X., Revhaug, I., Xia, H., Zhu, Z., & Kumar, L. (2015). Optimization of Causative Factors for Landslide Susceptibility Evaluation Using Remote Sensing and GIS Data in Parts of Niigata Japan. *PLOS ONE*, *10*(7), e0133262. https://doi.org/10.1371/journal.pone.0133262

Drăguţ, L., Csillik, O., Eisank, C., & Tiede, D. (2014). Automated parameterisation for multi-scale image segmentation on multiple layers. *ISPRS Journal of Photogrammetry and Remote Sensing, 88*, 119–127. https://doi.org/10.1016/j.isprsjprs.2013.11.018

Drusch, M., Del Bello, U., Carlier, S., Colin, O., Fernandez, V., Gascon, F., & Bargellini, P. (2012). Sentinel-2: ESA's optical high-resolution mission for GMES operational

services. *Remote Sensing of Environment, 120*, 25–36. https://doi.org/10.1016/j.rse.2011.11.026

Duro, D. C., Franklin, S. E., & Dubé, M. G. (2012). Multi-scale object-based image analysis and feature selection of multi-sensor earth observation imagery using random forests. International Journal of Remote Sensing, 33(14), 4502–4526. https://doi.org/10.1080/01431161.2011.649864

eCognition Developer, T. (2014). 9.0 user guide. Trimble Germany GmbH: Munich, Germany.

Guzzetti, F., Carrara, A., Cardinali, M., & Reichenbach, P. (1999). Landslide hazard evaluation: A review of current techniques and their application in a multi-scale study. *Central Italy. Geomorphology, 31*(1), 181–216. https://doi.org/10.1016/S0169-555X(99)00078-1

Guzzetti, F., Mondini, A. C., Cardinali, M., Fiorucci, F., Santangelo, M., & Chang, K. T. (2012). Landslide Inventory Maps: New Tools for an Old Problem. *112*(1–2), 42–66. https://doi.org/10.1016/j.earscirev.2012.02.001

Huete, A. R. (1988). A soil-adjusted vegetation index (SAVI). *Remote Sensing of Environment*, *25*(3), 295–309. https://doi.org/10.1016/0034-4257(88)90106-X

Kamp, U., Growley, B. J., Khattak, G. A., & Owen, L. A. (2008). GIS-based landslide susceptibility mapping for the 2005 Kashmir earthquake region. *Geomorphology, 101*(4), 631–642.

Kamp, U., Owen, L. A., Growley, B. J., & Khattak, G. A. (2010). Back analysis of landslide susceptibility zonation mapping for the 2005 Kashmir earthquake: An assessment of the reliability of susceptibility zoning maps. *Natural Hazards, 54*(1), 1–25. https://doi.org/10.1007/s11069-009-9451-7

Keyport, R. N., Oommen, T., Martha, T. R., & Sajinkumar, K. (2018). A comparative analysis of pixel-and object-based detection of landslides from very high-resolution images. *International Journal of Applied Earth Observation and Geoinformation, 64*, 1–11. https://doi.org/10.1016/j.jag.2017.08.015

Khan, S. F., Kamp, U., & Owen, L. A. (2013). Documenting five years of landsliding after the 2005 Kashmir earthquake, using repeat photography. *Geomorphology, 197*, 45–55. https://doi.org/10.1016/j.geomorph.2013.04.033

Khattak, G. A., Owen, L. A., Kamp, U., & Harp, E. L. (2010). Evolution of earthquake-triggered landslides in the Kashmir Himalaya, northern Pakistan. *Geomorphology, 115*(1–2), 102–108. https://doi.org/10.1016/j.geomorph.2009.09.035

Kirschbaum, D., Stanley, T., & Zhou, Y. (2015). Spatial and temporal analysis of a global landslide catalog. *Geomorphology, 249*, 4–15. https://doi.org/10.1016/j.geomorph.2015.03.016

Lahousse, T., Chang, K. T., & Lin, Y. H. (2011). Landslide mapping with multi-scale object-based image analysis – a case study in the Baichi watershed Taiwan. *Natural Hazards and Earth System Sciences*, *11*(10), 2715–2726. https://doi.org/10.5194/nhess-11-2715-2011

Li, W., Du, Z., Ling, F., Zhou, D., Wang, H., Gui, Y., & Zhang, X. J. R. S. (2013). A comparison of land surface water mapping using the normalized difference water index from TM, ETM+ and ALI. *5*(11), 5530–5549.

Li, X., Cheng, X., Chen, W., Chen, G., & Liu, S. (2015). Identification of forested landslides using LiDar data, object-based image analysis, and machine learning algorithms. *Remote Sensing, 7*(8), 9705–9726. https://doi.org/10.3390/rs70809705

Lu, P., Stumpf, A., Kerle, N., & Casagli, N. (2011). Object-oriented change detection for landslide rapid mapping. *IEEE Geoscience and Remote Sensing Letters, 8*(4), 701–705. https://doi.org/10.1109/LGRS.2010.2101045

Mahmood, I., Qureshi, S. N., Tariq, S., Atique, L., & Iqbal, M. F. (2015). Analysis of landslides triggered by October 2005. *Kashmir Earthquake. Plos Currents*. https://doi.org/10.1371/currents.dis.0bc3ebc5b8adf5c7fe9fd3d702d44a99

Martha, T. R., Kerle, N., Jetten, V., van Westen, C. J., & Kumar, K. V. (2010). Characterising spectral, spatial and morphometric properties of landslides for semi-automatic detection using object-oriented methods. *Geomorphology, 116*(1–2), 24–36. https://doi.org/10.1016/j.geomorph.2009.10.004

Martha, T. R., van Westen, C. J., Kerle, N., Jetten, V., & Vinod Kumar, K. (2013). Landslide hazard and risk assessment using semi-automatically created landslide inventories. *Geomorphology, 184*, 139–150. https://doi.org/10.1016/j.geomorph.2012.12.001

Mezughi, T. H., Akhir, J. M., Rafek, A. G., & Abdullah, I. (2011). Landslide susceptibility assessment using frequency ratio model applied to an area along the EW highway (Gerik-Jeli). *American Journal of Environmental Sciences, 7*(1), 43. https://doi.org/10.3844/ajessp.2011.43.50

Mora, O. E., Lenzano, M. G., Toth, C. K., Grejner-Brzezinska, D. A., & Fayne, J. V. (2018). Landslide change detection based on multi-temporal airborne LiDAR-derived DEMs. *Geosciences, 8*(1), 23. https://doi.org/10.3390/geosciences8010023

Owen, L. A., Kamp, U., Khattak, G. A., Harp, E. L., Keefer, D. K., & Bauer, M. A. (2008). Landslides triggered by the 8 October 2005 Kashmir earthquake. *Geomorphology, 94*(1–2), 1–9. https://doi.org/10.1016/j.geomorph.2007.04.007

Qasim, M., Khan, M. A., & Haneef, M. (2014). Stratigraphic characterization of the Early Cambrian Abbottabad Formation in the Sherwan area, Hazara region, N. Pakistan: Implications for Early Paleozoic stratigraphic correlation in NW Himalayas, Pakistan. *Himalayan Earth Sciences, 47*(1), 25.

Qingqing, H., Yu, M., Jingbo, C., Anzhi, Y., & Lei, L. (2017). Landslide change detection based on spatio-temporal context. Paper presented at the IEEE International Geoscience and Remote Sensing Symposium (IGARSS).

Rehman, M. U., Zhang, Y., Meng, X., Su, X., Catani, F., Rehman, G., & Ahmad, I. (2020). Analysis of landslide movements using interferometric synthetic aperture radar: A case study in Hunza-Nagar Valley. *Pakistan. Remote Sensing, 12*(12), 2054. https://doi.org/10.3390/rs12122054

Saba, S. B., van der Meijde, M., & van der Werff, H. (2010). Spatiotemporal landslide detection for the 2005 Kashmir earthquake region. *Geomorphology, 124*(1), 17–25. https://doi.org/10.1016/j.geomorph.2010.07.026

Sato, H. P., Hasegawa, H., Fujiwara, S., Tobita, M., Koarai, M., Une, H., & Iwahashi J. (2007). Interpretation of landslide distribution triggered by the 2005 Northern Pakistan

earthquake using SPOT 5 imagery. *Landslides*, *4*(2), 113–122. https://doi.org/10.1007/s10346-006-0069-5

Shafique, M. (2020a). Spatial and temporal evolution of co-seismic landslides after the 2005 Kashmir earthquake. *Geomorphology*. https://doi.org/10.1016/j.geomorph.2020.107228

Shafique, M. (2020b). Spatial and temporal evolution of co-seismic landslides after the 2005 Kashmir earthquake. *Geomorphology, 362*, 107228.

Smith, A. (2010). Image segmentation scale parameter optimization and land cover classification using the Random Forest algorithm. *Journal of Spatial Science, 55*(1), 69–79. https://doi.org/10.1080/14498596.2010.487851

Stumpf, A., Malet, J.-P., & Delacourt, C. (2017a). Correlation of satellite image time-series for the detection and monitoring of slow-moving landslides. *Remote Sensing of Environment, 189*, 40–55. https://doi.org/10.1016/j.rse.2016.11.007

Stumpf, A., Marc, O., Malet, J. -P., & Michea, D. (2017b). Sentinel-2 for rapid operational landslide inventory mapping, 23–28 April 2017. Paper presented at the EGU General Assembly Conference.

Van Westen, C., Van Asch, T. W., & Soeters, R. (2006). Landslide hazard and risk zonation—Why is it still so difficult? *Bulletin of Engineering Geology and the Environment, 65*(2), 167–184. https://doi.org/10.1007/s10064-005-0023-0

Wang, H., Zhang, L., Yin, K., Luo, H., & Li, J. (2021). Landslide identification using machine learning. *Geoscience Frontiers, 12*(1), 351–364. https://doi.org/10.1016/j.gsf.2020.02.012

Yang, W., Qi, W., Wang, M., Zhang, J., & Zhang, Y. (2017). Spatial and temporal analyses of post-seismic landslide changes near the epicentre of the Wenchuan earthquake. *Geomorphology, 276*, 8–15. https://doi.org/10.1016/j.geomorph.2016.10.010

Yang, W., Wang, Y., Sun, S., Wang, Y., & Ma, C. (2019). Using Sentinel-2 time series to detect slope movement before the Jinsha River landslide. *Landslides, 16*(7), 1313–1324. https://doi.org/10.1007/s10346-019-01178-8

Yue, J., Tian, Q., Tang, S., Xu, K., & Zhou, C. (2019). A dynamic soil endmember spectrum selection approach for soil and crop residue linear spectral unmixing analysis. *International Journal of Applied Earth Observation and Geoinformation*, *78*, 306–317. S0303243418306937. https://doi.org/10.1016/j.jag.2019.02.001